Frequency-resolved measurement of the orbital angular momentum spectrum of femtosecond ultra-broadband optical-vortex pulses based on field reconstruction

2014 New J. Phys. 16 053020

(http://iopscience.iop.org/1367-2630/16/5/053020)

New Journal of Physics
The open access journal at the forefront of physics
Deutsche Physikalische Gesellschaft DPG | IOP Institute of Physics

Frequency-resolved measurement of the orbital angular momentum spectrum of femtosecond ultra-broadband optical-vortex pulses based on field reconstruction

Keisaku Yamane, Zhili Yang, Yasunori Toda and Ryuji Morita
Department of Applied Physics, Hokkaido University, Kita-13, Nishi-8, Kita-ku, Sapporo, 060-8628, Japan
and
JST, CREST, Japan
E-mail: morita@eng.hokudai.ac.jp

Received 10 December 2013, revised 28 February 2014
Accepted for publication 19 March 2014
Published 7 May 2014
New Journal of Physics **16** (2014) 053020
doi:10.1088/1367-2630/16/5/053020

Abstract
We propose a high-precision method for measuring the orbital angular momentum (OAM) spectrum of ultra-broadband optical-vortex (OV) pulses from fork-like interferograms between OV pulses and a reference plane-wave pulse. It is based on spatial reconstruction of the electric fields of the pulses to be measured from the frequency-resolved interference pattern. Our method is demonstrated experimentally by obtaining the OAM spectra for different spectral components of the OV pulses, enabling us to characterize the frequency dispersion of the topological charge of the OAM spectrum by a simple experimental setup. Retrieval is carried out in quasi-real time, allowing us to investigate OAM spectra dynamically. Furthermore, we determine the relative phases (including the sign) of the topological-charge-resolved electric-field amplitudes, which are significant for evaluating OVs or OV pulses with arbitrarily superposed modes.

Keywords: optical vortex, ultrashort pulse, orbital angular momentum spectrum, ultra-broadband pulse

1. Introduction

During the last decade, optical vortices (OVs) have been enthusiastically studied because of interest in the spatial phase of an electromagnetic wave changing linearly, over its cross-section, with the azimuthal angle ϕ around the beam center. This phase dependence leads to a phase singularity in the center, where there is zero field [1]. The phase profile is characterized by a factor of $\exp\left(im\phi\right)$, where $m\hbar$ indicates the orbital angular momentum (OAM) per photon [2]. Here, m, the topological charge, can be any integer value, providing a new degree of freedom in phase control. The study of these unique properties of OVs has attracted enormous attention because of increasing applications in many fields, such as optical trapping [3, 4] (especially, trapping for atom Bose–Einstein condensates [5, 6]) or manipulation [7, 8], optical telecommunications [9, 10], super-resolution microscopy [11–13], quantum information processing [14, 15], nulling interferometry for extra-solar planet searches [16] and nonlinear spectroscopy [17, 18].

Since preceding research mainly concentrated on the spatial field distribution of OVs, for most cases temporally-continuous OVs have been used so far. In contrast, we have recently demonstrated the generation of ultra-broadband OV pulses [19] and few-cycle ultrashort OV pulses [20] for applications in ultra-broadband/ultrafast nonlinear spectroscopy and high-peak power field interactions with matter.

The topological charge m describes the essential quantum character of OVs or OV pulses as well as their phase distribution. However, in many cases, these features have been so far investigated by observing fork-dislocation lines [21] or spiral patterns [22] in interferograms, dark lines using a cylindrical lens [23]/a tilted convex lens [24], or triangular-diffraction patterns [25]. Thus, while only the dominant topological charges have been determined, the purity or distribution of topological charge has not been discussed. Computer-generated holograms and spatial filtering has been utilized for obtaining OAM spectra mainly for continuous OVs rather than for dominant topological charge [14]. However, this is not suitable for ultra-broadband OV pulses because of inevitable angular dispersion from the diffraction effect of holograms on spatial light modulators (SLMs). To avoid the problem of this method for ultra-broadband OV pulses, one needs massive band-pass filters introduced in front of the SLMs and the adjustment of wavelength-dependent spatial filtering owing to spatial dispersion, which is far from practical. Hence, for OV pulses, the purity in its broad spectral region and the frequency dispersion relation of the topological charge m have not been quantitatively evaluated. For applications such as quantum information processing or ultrafast nonlinear spectroscopy by ultrashort OV pulses [17], frequency-resolved measurement of OAM spectrum and evaluation of topological-charge dispersion is crucial. In addition, determining the relative phases between electric-field amplitudes of each m component, which is important for evaluating OVs or OV pulses with arbitrarily superposed modes [26–28], is also quite difficult with previous methods.

In the present paper, we demonstrate an interferometric method of measurement of the OAM spectrum of ultra-broadband OV pulses based on field reconstruction by using the spatial Fourier transform. Our new method overcomes the drawbacks, such as angular dispersions for ultra-broadband pulses, of previous topological charge measurement methods. It also enables quantitative evaluation of the frequency-resolved OAM spectra

(distribution of topological charge as a function of frequency) and the measurement of topological-charge dispersion for ultra-broadband OV pulses.

Our measurements are composed of two principal steps. The first one is based on reconstruction of the field information (phase and amplitude) of the OV pulses to be measured. After selection of a desired wavelength component sliced from the whole spectral region of the OV pulses, it interferes with the correspondent tilted (quasi-) plane wave, forming an interferogram where the field information of the OV pulses for this spectral component is preserved. The field distribution can be reconstructed by Fourier-transforming and filtering a certain part out of the two-dimensional spatial frequency domain of the interferogram and performing an inverse Fourier transform of this part, as referred to as Takeda's method [29]. Field reconstruction for observing the OV structure has been previously done from many interference images with different phase offsets between an OV and a plane wave [30]. In contrast, our electric-field reconstruction using the spatial Fourier transform needs only one interference pattern between an OV and a tilted plane wave.

Next, making use of the Fourier-relationship between the azimuthal angle ϕ and topological charge m [31], we are able to obtain the OAM spectrum of the electric-field amplitude as a function of the radial coordinate r as well as m, by projecting the reconstructed field (in spatial coordinates: r and ϕ) onto the topological charge domain. Here it is worth mentioning that, in particular, this step of our method enables the evaluation of the relative phases (including the positive or negative sign) of topological-charge-resolved electric-field amplitudes, which is difficult by the use of previous methods. After squaring the absolute value of this OAM spectrum of electric-field amplitude for each m, the power spectrum of the OAM for this spectral component of the OV pulses can finally be obtained by integration of the squared absolute value with respect to r. By our simple experimental setup, which is designed to control the selected position and bandwidth in the whole spectral region of the input to form the interferogram, the frequency-resolved OAM spectra of the OV pulses in the wavelength range are acquired as a function of topological charge m and wavelength λ. Thus, the topological-charge dispersion can also be obtained for each m from this three-dimensional spectrum (power spectrum as a function of m and λ).

2. Proposed method

The complex electric field of the ultra-broadband Laguerre–Gaussian OV pulses, with the superposition of modes of topological charges m and radial indices p ($\mathrm{LG}_p{}^m$ modes), propagating in z-direction, can be expressed by

$$E(r, \phi, z, t) = \int_{-\infty}^{\infty} \mathrm{d}\omega \sum_{p=0}^{\infty} \sum_{m=-\infty}^{\infty} c_{m,p}(\omega)\, u_{m,p}(r, \phi, z, \omega) \exp\left\{\mathrm{i}\left[k(\omega)z - \omega t\right]\right\}, \tag{1}$$

where $c_{m,p}(\omega)$ represents a complex mode coefficient, r is the radius from the beam center, ϕ is the azimuthal angle in the cross-section, t is the time, ω is the angular-frequency, and $k(\omega)$ is the wave number as a function of ω. The function $u_{m,p}(r, \phi, z, \omega)$ of a $\mathrm{LG}_p{}^m$ mode is given by

$$u_{m,p}(r,\phi,z,\omega) = \sqrt{\frac{2p!}{\pi(p+|m|)!}}\left[\frac{\sqrt{2}r}{w(z)}\right]^{|m|} L_p^{|m|}\left(\frac{2r^2}{w(z)^2}\right)\frac{w_0}{w(z)} \times \exp\left[-\frac{r^2}{w(z)^2} - \mathrm{i}\frac{kr^2}{2R(z)} + \mathrm{i}m\phi - \mathrm{i}\Phi_G(z)\right], \quad (2)$$

where $L_p^{|m|}(x)$ is the generalized Laguerre polynomial defined by

$$L_p^{|m|}(x) = \sum_{n=0}^{p}(-1)^n\binom{p+|m|}{p-n}\frac{x^n}{n!}. \quad (3)$$

Parameters $R(z)$ and $w(z)$ denote the radius of curvature of wavefronts and the beam size for the Gaussian mode ($p = m = 0$) at a propagation distance z, as expressed by

$$R(z) = \left(z_R^2 + z^2\right)/z, \qquad w(z) = w_0\sqrt{1 + z^2/z_R^2}, \quad (4)$$

with the Rayleigh range

$$z_R = kw_0^2/2. \quad (5)$$

The constant w_0 is the beam waist. The parameter $\Phi_G(z)$ denotes the Gouy phase, which is known to be an additional phase shift for a focused and propagated beam, differing from that for a plane wave.

$$\Phi_G(z) = \left(2p + |m| + 1\right)\Phi(z) \equiv \left(2p + |m| + 1\right)\arctan\left(z/z_R\right), \quad (6)$$

where $\Phi(z)$ is the fundamental Gouy phase for the Gaussian mode. Here, for simplicity, we use the expressions k, $R(z)$, $w(z)$, w_0, z_R, $\Phi(z)$ and $\Phi_G(z)$, although they are functions of ω.

Only for purpose of describing the principle of our proposed method, we use, for convenience, a continuous wave (with a frequency of ω) by omitting the integration with respect to ω in equation (1). So the electric field of the OV then becomes

$$E(r,\phi,z,t) = \sum_{p=0}^{\infty}\sum_{m=-\infty}^{\infty} A_{m,p}(r,z)\exp\left[\mathrm{i}(kz - \omega t + m\phi)\right], \quad (7)$$

where $A_{m,p}(r,z)$ is defined by

$$A_{m,p}(r,z) = c_{m,p}\sqrt{\frac{2p!}{\pi(p+|m|)!}}\left[\frac{\sqrt{2}r}{w(z)}\right]^{|m|} L_p^{|m|}\left(\frac{2r^2}{w(z)^2}\right)\frac{w_0}{w(z)} \times \exp\left[-\frac{r^2}{w(z)^2} - \mathrm{i}\frac{kr^2}{2R(z)} - \mathrm{i}\Phi_G(z)\right]. \quad (8)$$

Here, we express $c_{m,p}(\omega)$ by $c_{m,p}$ for simplicity. The OV interferes at a distance $z = z_0$ with a reference plane wave $E_{ref}(r,\phi,z,t)$ expressed by

$$E_{ref}(r,\phi,z,t) = B\exp\left[\mathrm{i}\left(k_{0z}z - k_{0y}y - \omega t + \alpha_0\right)\right]. \quad (9)$$

This reference wave has a wave vector $\mathbf{k}_0 = \left(0, -k_{0y}, k_{0z}\right)$ and the same frequency ω as in equation (7), which is tilted by angle θ (angle between $\mathbf{k}_0$ and $-y$-axis). Here $k_{0z} = k\cos\theta$, $k_{0y} = k\sin\theta$, $y = r\sin\phi$, α_0 is the constant phase, and B is a constant amplitude. Setting $\beta_0 = \left(k - k_{0z}\right)z_0 - \alpha_0$, the interferogram $I_{\text{interf}}\left(r, \phi\right)$ after time-averaging becomes

$$I_{\text{interf}}\left(r, \phi\right) \propto |B|^2 + \sum_{p=0}^{\infty}\sum_{m=-\infty}^{\infty}\left|A_{m,p}\left(r, z_0\right)\right|^2 + 2\sum_{p=0}^{\infty}\sum_{m=-\infty}^{\infty}A_{m,p}\left(r, z_0\right)B^* \exp\left[\mathrm{i}\left(m\phi + k_{0y}y + \beta_0\right)\right] + \text{c.c.}, \tag{10}$$

where the symbol * denotes the complex conjugate. By two-dimensional Fourier transformation into the spatial frequency domain of k_x and k_y, three peaks appear at $(k_x = 0, k_y = \pm k_{0y})$ and $(k_x = 0, k_y = 0)$. After filtering out only the peak appearing at $(k_x = 0, k_y = k_{0y})$, we apply the inverse Fourier transformation to this term and obtain the + AC part of the interferogram $I_{\text{AC}+}\left(r, \phi\right)$ as

$$I_{\text{AC}+}\left(r, \phi\right) \propto \sum_{p=0}^{\infty}\sum_{m=-\infty}^{\infty}A_{m,p}\left(r, z_0\right)B^* \exp\left[\mathrm{i}\left(m\phi + k_{0y}y + \beta_0\right)\right]. \tag{11}$$

Here β_0 is constant, hence multiplying the value of $\exp\left(-\mathrm{i}k_{0y}y\right)$, which is only related to tilted angle θ, on both sides of the equation (11), we find, by changing the dummy index m to m',

$$I_{\text{AC}+}\left(r, \phi\right)\exp\left(-\mathrm{i}k_{0y}y\right) \propto B^*\sum_{p=0}^{\infty}\sum_{m'=-\infty}^{\infty}A_{m',p}\left(r, z_0\right)\exp\left(\mathrm{i}m'\phi\right) \equiv \sum_{p=0}^{\infty}F_p\left(r, \phi\right). \tag{12}$$

Since B is a constant amplitude, the field $\sum_{p=0}^{\infty}F_p\left(r, \phi\right)$, proportional to the electric field of the OV to be measured, is finally obtained as a function of r and ϕ.

For the next main step, we first compute a complex inner product $D_m\left(r\right)$ between the reconstructed field $\sum_{p=0}^{\infty}F_p\left(r, \phi\right)$ and $\exp\left(\mathrm{i}m\phi\right)$ (m are integers from −16 to 15 in our analysis) expressed by

$$D_m\left(r\right) = \frac{1}{2\pi}\sum_{p=0}^{\infty}\int_0^{2\pi}F_p\left(r, \phi\right)\exp\left(-\mathrm{i}m\phi\right)\mathrm{d}\phi, \tag{13}$$

which represents the OAM spectrum of the electric field. It should be noted that the present method can retrieve both the topological-charge-resolved amplitude and phase of the OV. Although the mode decomposition concerning indices p can be performed, we here focus only OAM-resolution, that is a decomposition to m modes. Hence, we examine m-resolved electric fields with the superposition of p modes. Simultaneous m- and p-mode decompositions will be discussed elsewhere.

Next, we carry out the integration of $\left|D_m\left(r\right)\right|^2$ for each m with respect to r in order to obtain the OAM power spectrum S_m for the OV expressed by equation (7), that is,

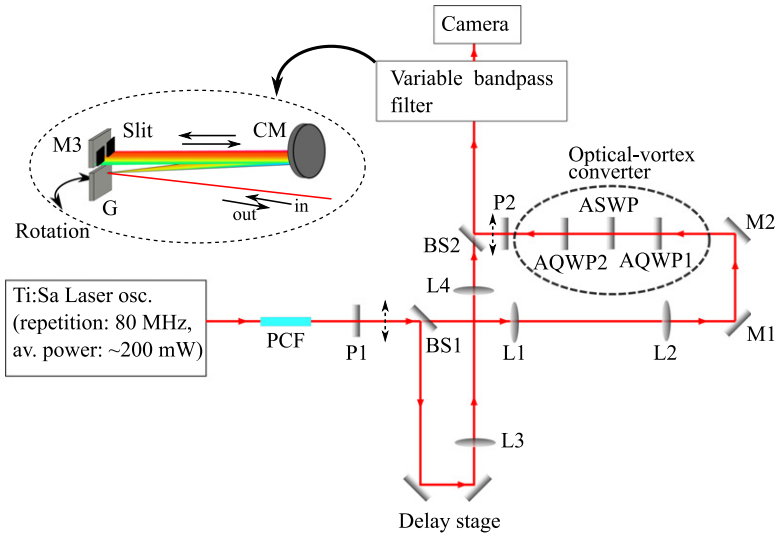

Figure 1. Schematic of the experimental setup for frequency-resolved measurement of the orbital-angular momentum spectrum of ultra-broadband optical vortex pulses. PCF: photonic crystal fiber, P1, 2: linear polarizers, BS1, 2: beam splitters, L1–L4: achromatic convex lenses, M1–3: mirrors, AQWP1, 2: achromatic quarter-wave plates, ASWP: axially-symmetric wave plate, G: grating, CM: concave mirror.

$$S_m = 2\pi \int_{r_{\min}}^{r_{\max}} \left| D_m(r) \right|^2 r \mathrm{d}r. \tag{14}$$

Here, the maximum radius $r_{\max}$ is selected to assure that the part containing field information is included, and the minimum radius $r_{\min}$ is determined by interpolation.

For ultra-broadband pulses, S_m can be rewritten as $I_m(\omega)$ as a function of topological charge m and angular frequency ω, since this procedure of continuous OV involves obtaining the OAM spectrum corresponding to a certain frequency in the broadband OV pulses described by equations (1) and (2). By repeating the calculation above for various spectral components, the frequency- or wavelength-resolved OAM spectra of OV pulses composed of the OAM spectra at different angular frequencies or wavelengths are acquired.

3. Experimental setup

In our experiment, a mode-locked Ti:sapphire laser oscillator is used as a light source (center wavelength: ~800 nm, repetition rate: ~80 MHz). Femtosecond pulses from the oscillator are focused into a photonic crystal fiber (PCF; core diameter 2.3 μm, length: ~30 mm, zero-dispersion wavelength: 790 nm) to broaden their spectra (bandwidth: ~600–~950 nm). As shown in figure 1, a linearly-polarized ultra-broadband pulse from the PCF is split into two pulses in separate arms by a beam splitter (BS1). One beam passes through a pair of achromatic convex lenses with focal lengths of $f_1 = 200$ and $f_2 = 100$ mm, and its beam size shrinks by a factor of 1/2. Then this beam is converted into ultra-broadband OV pulses, with nominal topological charge of $m = 2$ and made up of a superposition of radial modes with indices p, by the use of an ultra-broadband OV converter (composed of an axially-symmetric wave plate

ASWP and two quarter-wave plates AQWP1 and 2), in a way identical to our previous work [20]. The other beam is magnified by a pair of achromatic convex lenses (focal lengths $f_3 = 100$ and $f_4 = 200$ mm) by a factor of 2, for use as a reference quasi-plane wave in comparison with the shrunk beam above. The two beams are interferometrically recombined by another beam splitter (BS2), which can also control the interference angle (set to be $\sim 0.25°$ in the present experiment) between these two arms.

Instead of using many band-pass filters to obtain interferograms at different wavelength components, which is not practical for ultra-broadband pulses, here we introduce a reflective grating G (groove density $N = 235\,\mathrm{mm}^{-1}$) to convert different wavelengths to correspondent spatial frequencies. We filter out a certain wavelength component by putting a width-adjusted slit at the focal image plane of a concave mirror (radius of curvature $R = -500$ mm) and by rotating the grating G. By this experimental setup, only the desired component in the whole spectrum is reflected back by a slightly-tilted mirror positioned accurately behind the slit to form an interferogram which is detected by a charge-coupled device (CCD) camera. This experimental setup realizes full control of the position and the bandwidth of the wavelength range by allowing the adjustment of the slit width and rotation of the grating, which is essential for frequency-resolved OAM measurements for ultra-broadband OV pulses. Moreover, we incorporate a newly-built software that enables quasi-real-time measurement (acquisition and processing rate is higher than $2\,\mathrm{s}^{-1}$ even for a high resolution camera with 2560×1920 pixels). This enables the inspection of a calculated OAM spectrum dynamically and more reliably in real-time, as shown below.

4. Results and discussion

Figure 2(a) shows the interferogram centered at 700 nm (bandwidth: ~ 10 nm) between a generated nominally-pure ($m = 2$) ultra-broadband OV pulse and a tilted quasi-plane-wave pulse. The intensity and phase profiles, reconstructed by the procedure described in section 2, are respectively shown in figures 2(b) and (c). We find that both the intensity and phase profiles are clearly reconstructed, the former of which closely resembles the directly measured intensity profile shown in figure 2(f). The retrieved intensity profile was compared with the directly measured intensity profile by a CCD camera, giving a mean-squared error G of $\sim 10^{-4}$, as listed in table 1. This indicates that our reconstruction is excellent. The mean-squared error (per-pixel error) G is defined [32] by

$$G = \frac{1}{NM}\sum_{i=1}^{N}\sum_{j=1}^{M}\left(I_{ij}^{\mathrm{retr}} - I_{ij}^{\mathrm{meas}}\right)^2 \tag{15}$$

where I_{ij}^{retr} and I_{ij}^{meas} are the retrieved and directly-measured intensity profiles (normalized to have unity peak) at (i, j) pixel ($N = 2560$, $M = 1920$), respectively. The error is considered to be mainly due to the speckle in the directly measured intensity profile, which exhibits a more sensitive dependence in this profile than in the interferogram. The reconstructed phase profile shows the azimuthal phase dependence clearly with topological charge of $m = 2$.

From the reconstructed field, the OAM spectrum of the electric-field amplitude $\sum_{p=0}^{\infty} A_{m,p}\left(r, z_0\right)$ was calculated. Figure 2(d) denotes $\left|\sum_{p=0}^{\infty} A_{m,p}\left(r, z_0\right)\right|$ (a real number as a

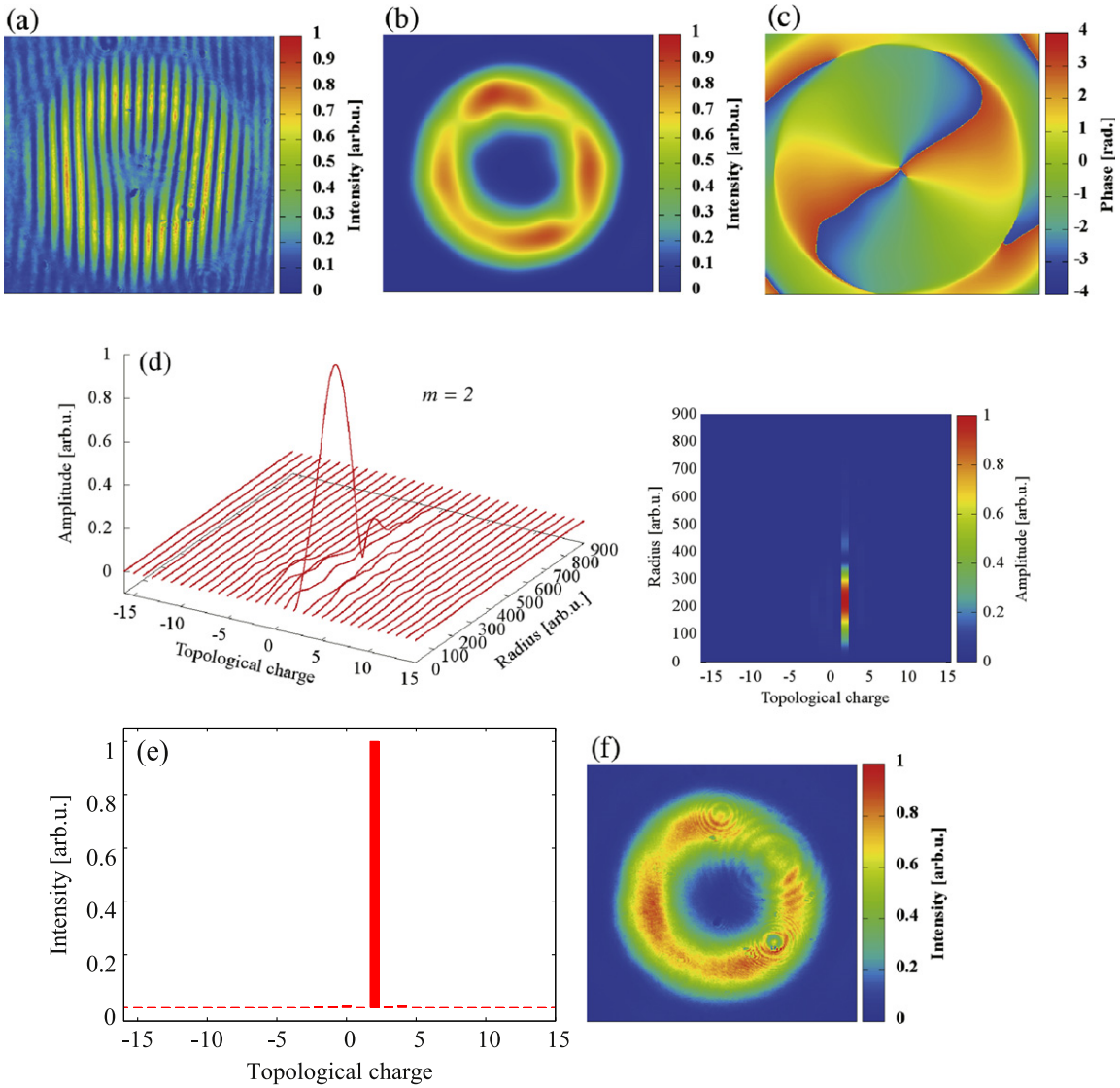

Figure 2. (a) Captured interferogram between an OV pulse and a quasi-plane wave pulse. (b) Reconstructed intensity and (c) phase profiles of the OV pulse, (d) computed OAM spectrum of electric-field amplitude $\left|\sum_{p=0}^{\infty} A_{m,\,p}\left(r,\,z_0\right)\right|$ (right: contour plot) and (e) evaluated OAM power spectrum centered at ~700 nm. (f) Directly-measured intensity profile corresponding to (b).

function of r) at ~700 nm (its top view is plotted on the right side). This indicates that the $m = 2$ azimuthal mode is dominant compared with the small side azimuthal modes. From the fact that $\left|\sum_{p=0}^{\infty} A_{m=2,\,p}\left(r,\,z_0\right)\right|$ manifests oscillatory behavior in r-direction, the $m = 2$ azimuthal mode is further decomposed into a dominant $p = 0$ mode and residual $p\left(\neq 0\right)$ modes. The OAM power spectrum obtained by integration through the above-mentioned procedure is presented in figure 2(e). The center position of the cylindrical polar coordinates was carefully selected to minimize the variance of the OAM spectrum, which is also calculated

Table 1. Evaluated mean-squared errors G for retrieved results in the measured wavelength range.

Center wavelength (nm)	Error G
650	1.184×10^{-4}
700	2.203×10^{-4}
750	1.239×10^{-3}
800	1.075×10^{-3}
850	1.564×10^{-3}
900	2.706×10^{-4}
700 (half-cut)	9.744×10^{-5}

and displayed in our software in real time. This figure shows that the OV pulses to be measured possess a topological charge of $m = 2$ with very high contrast. Even though the optical power corresponding to contamination of m is below 1% compared with that of the dominant value of m, it can still be measured by our method.

By rotating the grating G, the OAM spectra at other wavelengths were also measured. Figures 3(a) and (e) show typical examples of interferograms of other spectral components (centered at 800 and 900 nm, respectively; bandwidths ~10 nm). As is often the cases with interference patterns between OVs ($|m| \geqslant 1$) and plane waves, we find that a singularity with $m = 2$ breaks into two singularities with $m = 1$. Even though a singularity breaks, electric-field reconstruction is well performed, as indicated in figures 3(b), (c), (f) and (g). It should be noted that the phase profiles reconstructed by our method clearly resolve the splitting of the singularities, as shown in figures 3(c) and (g). The OAM spectra at 800 and 900 nm are obtained as shown in figures 3(d) and (h), respectively, which are evaluated to be similar to that at 700 nm in our case. Whereas they show that the $m = 2$ modes are dominant with small side modes below 1%, the power ratios of the $m = 0$ modes to the $m = 2$ modes at 800 and 900 nm are higher than that at 700 nm. These higher power ratios cause the splitting of the singularities. The mean-squared errors G at 800 and 900 nm were evaluated to be $\sim 10^{-3}$ and $\sim 10^{-4}$, respectively, as listed in table 1. These results confirm that our generated ultra-broadband OV pulses possess a topological charge of $m = 2$ with considerably high contrast throughout their whole spectral region.

In order to further assess and evaluate our method, we introduce mixed-type OV pulses as inputs. The method we use here is spatially blocking half of the input OV pulses by a knife edge lying exactly along a diameter of the OV pulses (nominally $m = 2$), generated as in the previous step. Only the part with the π-range azimuthal angle of the pulse beam passes through and forms the interferogram with a reference quasi-plane wave pulse. The half-blocked OV pulse is no longer an eigenmode of the paraxial equation and the spatial window of azimuthal angle broadens the OAM spectrum of the original OV pulses [31, 33].

Figure 4(a) shows the interferogram centered at 700 nm (bandwidth: ~10 nm) of the mixed-type ultra-broadband OV pulses (m centered at 2). The reconstructed intensity and phase profiles are shown in figures 4(b) and (c), respectively. The results of half-blocked intensity and phase profiles (to the left of the solid lines) are well-reconstructed, in comparison with those to the left of the unblocked OV pulses shown in figures 2(b) and (c). The mean-squared error G was evaluated to be $\sim 10^{-4}$, as listed in table 1, giving nearly half the value of the unblocked

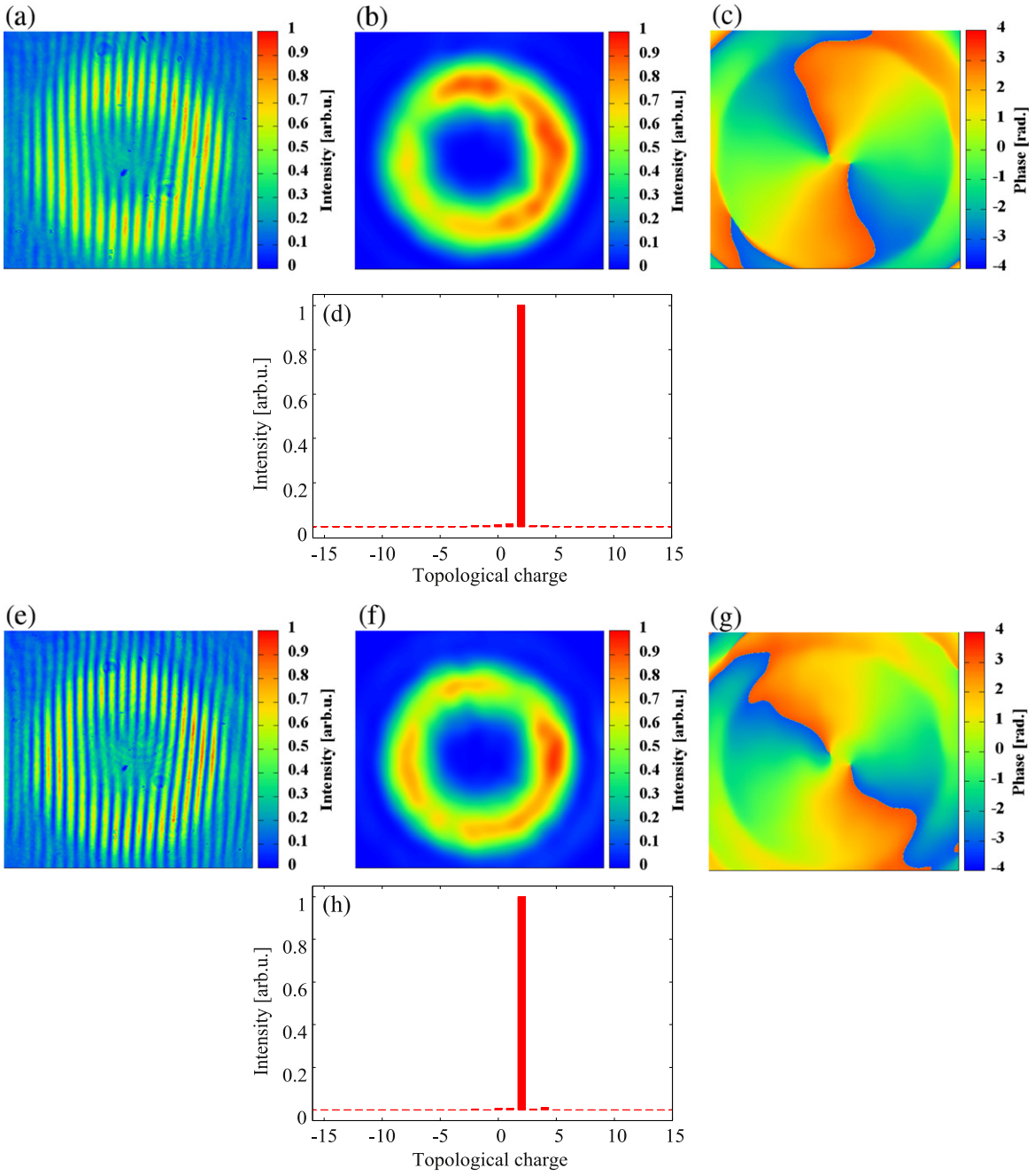

Figure 3. (a) Captured interferogram, (b) reconstructed intensity and (c) phase profiles of the OV pulse at ∼800 nm, together with (d) evaluated OAM power spectrum from (a). (e) Captured interferogram, (f) reconstructed intensity and (g) phase profiles of the OV pulse at ∼900 nm, together with (h) evaluated OAM power spectrum from (e).

case, which is reasonable. This is because almost null intensity was recorded in the half-portion of the measured region in the half-blocked case. Figure 4(d) shows the measured OAM power spectrum, together with the theoretically calculated result. The theoretical results take into consideration OAM spectral broadening (equivalently the diffraction effect) by half-blocking.

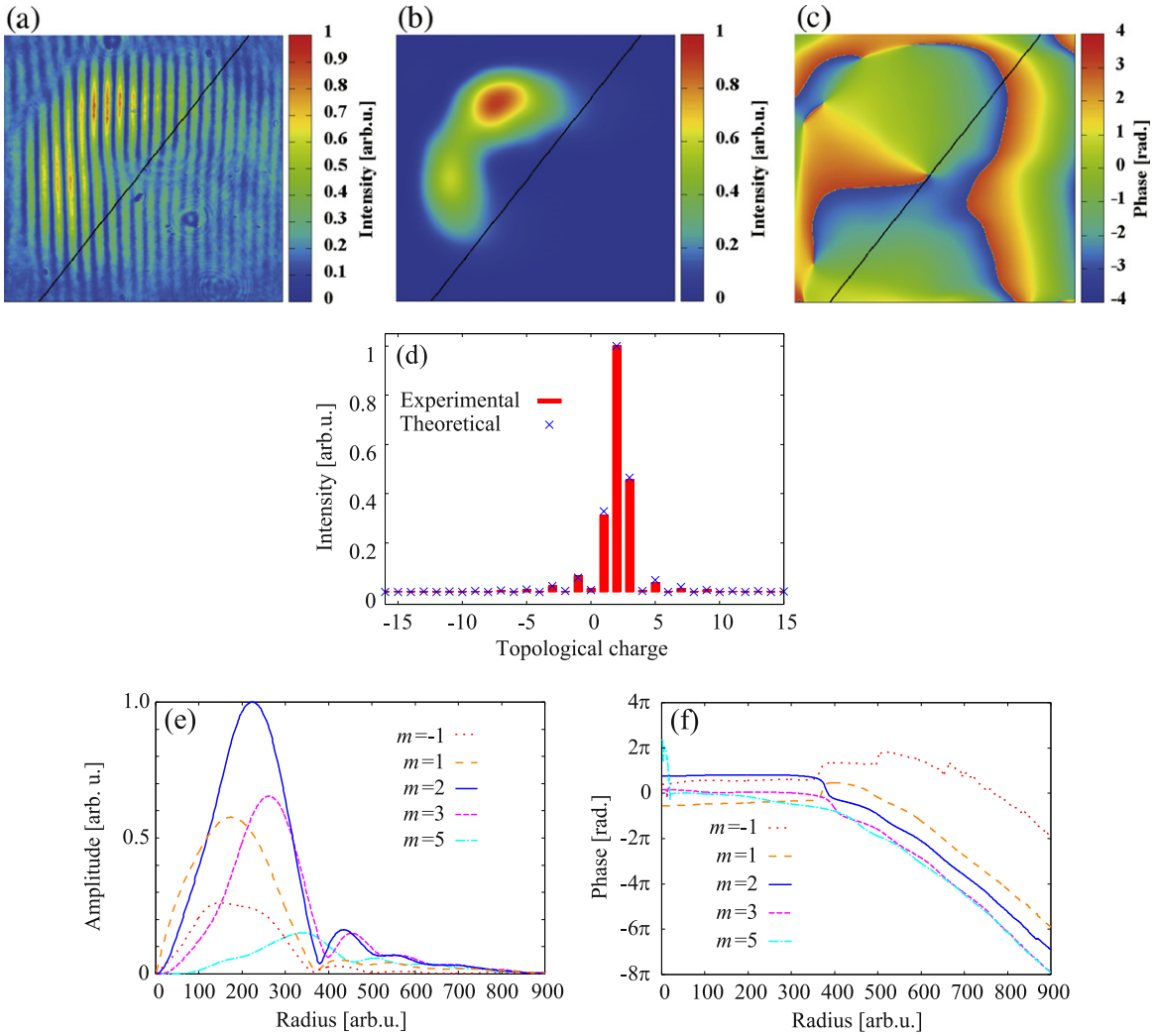

Figure 4. (a) Captured interferogram of a half-blocked OV pulse and a quasi-plane wave pulse, (b) reconstructed intensity and (c) phase profiles of the half-blocked OV pulse. Solid lines show the half-blocked boundary as a guide to the eye. (d) Measured OAM spectrum from interferogram (a), together with theoretical calculation by taking account of the diffraction effect, denoted by crosses. (e) The amplitudes and (f) the phases of the OAM-resolved electric fields $\sum_{p=0}^{\infty} A_{m,\,p}\left(r,\,z_0\right)$ for $m = -1,\ 1,\ 2,\ 3$ and 5, as functions of r.

The electric-field amplitude $\left|\sum_{p=0}^{\infty} A_{m,\,p}\left(r,\,z_0\right)\right|$ of mixed-type OV pulses is calculated from the convolution between that of the pure OV pulses and the sinc function (the Fourier transform of the unblocked window). The measured and calculated OAM power spectra in figure 4(d) well agree with each other, indicating that our method is useful and powerful for resolving OAM spectra of mixed-type ultra-broadband OV pulses as well as pure ultra-broadband OV pulses. Figures 4(e) and (f) show the computed amplitudes and phases of OAM-resolved electric fields $\sum_{p=0}^{\infty} A_{m,\,p}\left(r,\,z_0\right)$ as functions of r (camera pixel number), respectively, for $m = -1,\ 1,\ 2,\ 3$ and

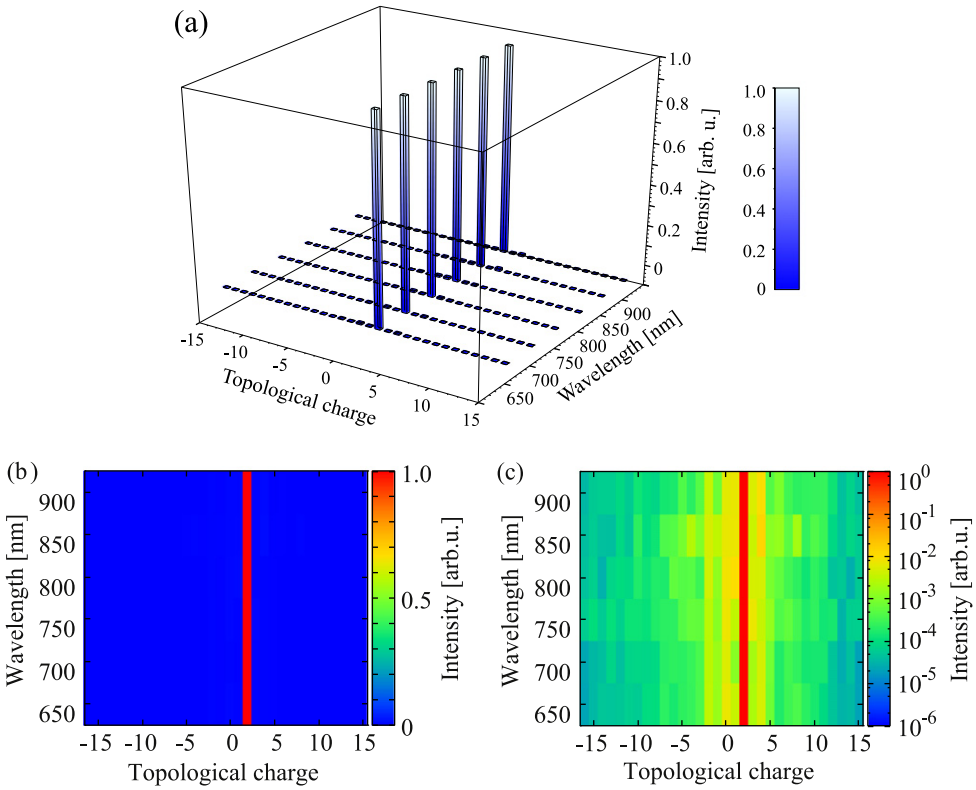

Figure 5. (a) Frequency-resolved OAM power spectrum from 650 to 900 nm. (b) and (c) show its contour plots in linear and log scales, respectively.

5 (dominant components of OAM power spectrum shown in figure 4(d)). In the *r*-region (∼15-∼350) where the OAM-resolved amplitudes are large (the inner ring region of OAM-resolved vortices), the phases are clearly well-defined, giving almost constant values (1.76, −1.32, 2.53, 0.157 and −0.466 rad for $m = -1$, 1, 2, 3 and 5, respectively). To our knowledge, this represents the first determination of the relative phases of OAM-resolved electric fields. This capability is important for characterizing OVs or OV pulses with arbitrarily superposed modes, for example fractional vortices [26, 27].

To analyze the frequency dispersion of OAM spectrum or topological-charge dispersion of ultra-broadband OV pulses, which is crucial for the previously-mentioned applications using OV pulses, we performed measurements of the frequency-resolved OAM spectrum ranging from 650 to 900 nm. By continuously rotating the grating G (using a spectrometer in front of the camera to simultaneously monitor the spectral information of an input), a series of normalized OAM spectra for consecutive spectral components were attained from the correspondent input interferograms. Figure 5(a) shows the measured frequency-resolved OAM spectrum in this wavelength range (sampling wavelength-spacing is 50 nm) as a function of topological charge m and wavelength λ of the OV pulses to be measured (also plotted in linear and log scales with interpolation for wavelength, as shown in figures 5(b) and (c), respectively). By slicing this spectrum with a m-constant plane, we are able to obtain the topological-charge dispersion, that is, the topological charge m as a function of wavelength or frequency. From figure 5, while topological-charge dispersion is sufficiently small in this case, our method, in general, enables one to characterize topological-charge dispersion even with such small

dispersion. In addition, our results support the fact that our previously-reported methods generating ultrashort or ultra-broadband OV pulses by using axially-symmetric polarizers or waveplates [19, 20] are free from topological-charge dispersion.

5. Conclusion

In conclusion, we have proposed and demonstrated a high-precision interferometric electric-field reconstruction method in the spatial domain, combined with frequency slicing, to obtain the frequency-resolved OAM power spectrum (topological charge distribution) of femtosecond ultra-broadband OV pulses ($\sim$600 – $\sim$950 nm). Our method is based on the spatial reconstruction of the electric-fields of the pulses to be measured from the frequency-resolved interference patterns. We experimentally applied this method to ultra-broadband OV pulses with nominally-pure topological charge. It is found that the electric fields in the spatial domain were reconstructed well, giving mean-squared errors of below $\sim 10^{-3}$ between the retrieved and directly-measured beam intensity profiles. The obtained OAM spectra gave high precision results, enabling us to even detect below 1% contamination. In our method, the retrieval proceeds in quasi-real time, allowing us to investigate the OAM spectra dynamically. Furthermore, the comparison with experimental and theoretical results (intensity/phase profiles and OAM spectra) for a half-blocked OV pulse confirms the reliability of our method. To our knowledge, this is the first demonstration of the determination of the relative phases of OAM-resolved electric fields. This capability of relative-phase determination is important for characterizing OVs or OV pulses with arbitrarily superposed modes. In addition, our method for providing the OAM- and frequency-resolved spectra enables us to access the frequency dispersion of the topological charge of the ultra-broadband OV pulses to be measured. Our measurement method should also prove practically applicable in related fields of research and application, such as ultrafast nonlinear spectroscopy and quantum information processing by ultra-broadband OV pulses.

Acknowledgments

This work was partially supported by Grant-in-Aid for Scientific Research (B) (No. 23360024, 2011–2014) from Japan Society for the Promotion of Science (JSPS).

References

[1] Nye J F and Berry M V 1974 Dislocations in wave trains *Proc. R. Soc.* A **336** 165
[2] Allen L, Beijersbergen M W, Spreeuw R J C and Woerdman J P 1992 Orbital angular momentum of light and the transformation of Laguerre–Gaussian laser modes *Phys. Rev.* A **45** 8185
[3] Ashkin A 1992 Forces of a single-beam gradient laser trap on a dielectric sphere in the ray optics regime *Biophys. J.* **61** 569
[4] Mehta A D, Rief M, Spudich J A, Smith D A and Simmons R M 1999 Single-molecule biomechanics with optical methods *Science* **283** 1689
[5] Kuga T, Torii Y, Shiokawa N, Hirano T, Shimizu Y and Sasada H 1997 Novel optical trap of atoms with a doughnut beam *Phys. Rev. Lett.* **78** 4713

[6] Wright E M, Arlt J and Dholakia K 2001 Toroidal optical dipole traps for atomic Bose–Einstein condensates using Laguerre–Gaussian beams *Phys. Rev.* A **63** 013608
[7] Simpson N B, Dholakia K, Allen L and Padgett M J 1997 Mechanical equivalence of spin and orbital angular momentum of light: an optical spanner *Opt. Lett.* **22** 52
[8] Paterson L, MacDonald M P, Arlt J, Sibbet W, Bryant P E and Dholakia K 2001 Controlled rotation of optically trapped microscopic particles *Science* **292** 912
[9] Lin J, Yuan X-C, Tao S H and Burge R E 2007 Multiplexing free-space optical signals using superimposed collinear orbital angular momentum states *Appl. Opt.* **46** 4680
[10] Bozinovic N, Yue Y, Ren Y, Tur M, Kristensen P, Huang H, Willner A E and Ramachandran S 2013 Terabit-scale orbital angular momentum mode division multiplexing in fibers *Science* **340** 1545
[11] Hell S W and Wichmann J 1994 Breaking the diffraction resolution limit by stimulated emission: stimulated-emission-depletion fluorescence microscopy *Opt. Lett.* **19** 780
[12] Willig K I, Rizzoli S O, Westphal V, Jahn R and Hell S W 2006 STED microscopy reveals that synaptotagmin remains clustered after synaptic vesicle exocytosis *Nature* **440** 935
[13] Iketaki Y, Watanabe T, Bokor N, Omatsu T, Hiraga T, Yamamoto K and Fujii M 2007 Measurement of contrast transfer function in super-resolution microscopy using Two-color Fluorescence Dip Spectroscopy *Appl. Spectrosc.* **61** 6
[14] Mair A, Vaziri A, Weihs G and Zeilinger A 2001 Entanglement of the orbital angular momentum states of photons *Nature* **412** 313
[15] Vaziri A, Weihs G and Zeilinger A 2002 Experimental two-photon, three-dimensional entanglement for quantum communication *Phys. Rev. Lett.* **89** 240401
[16] Swartzlander G A Jr., Ford E L, Abdul-Malik R S, Close L M, Peters M A, Palacios D M and Wilson D W 2008 Astronomical demonstration of an optical vortex coronagraph *Opt. Express* **16** 10200
[17] Tokizane Y, Shimatake K, Toda Y, Oka K, Tsubota M, Tanda S and Morita R 2009 Global evaluation of closed-loop electron dynamics in quasi-one-dimensional conductors using polarization vortices Opt. *Express* **17** 24198
[18] Shigematsu K, Toda Y, Yamane K and Morita R 2013 Orbital angular momentum spectral dynamics of GaN excitons excited by optical vortices *Japan J. Appl. Phys.* **52** 08JL08
[19] Tokizane Y, Oka K and Morita R 2009 Supercontinuum optical vortex pulse generation without spatial or topological-charge dispersion *Opt. Express* **17** 14517
[20] Yamane K, Toda Y and Morita R 2012 Ultrashort optical-vortex pulse generation in few-cycle regime *Opt. Express* **20** 18986
[21] Harris M, Hill C A, Tapster P R and Vaughan J M 1994 Laser modes with helical wave fronts *Phys. Rev.* A **49** 3119
[22] Carpentier A V, Michinel H, Salgueiro J R and Olivieri D 2008 Making optical vortices with computer-generated holograms *Am. J. Phys.* **76** 916
[23] Denisenko V, Shvedov V, Desyatnikov A S, Neshev D N, Krolikowski W, Volyar A, Soskin M and Kivshar Y S 2009 Determination of topological charges of polychromatic optical vortices *Opt. Express* **17** 23374
[24] Vaity P, Banerji J and Singh R P 2013 Measuring the topological charge of an optical vortex by using a tilted convex lens *Phys. Lett.* A **377** 1154
[25] Hickmann J M, Fonseca E J, Soares W C and Chávez-Cerda S 2010 Unveiling a truncated optical lattice associated with a triangular aperture using light's orbital angular momentum *Phys. Rev. Lett.* **105** 053904
[26] Götte J B, O'Holleran K, Preece D, Flossmann F, Franke-Arnold S, Barnett S M and Padgett M J 2008 Light beams with fractional orbital angular momentum and their vortex structure *Opt. Express* **16** 993
[27] Miyamoto K, Miyagi S, Yamada M, Furuki K, Aoki N, Okida M and Omatsu T 2011 Optical vortex pumped mid-infrared optical parametric oscillator *Opt. Express* **19** 12220
[28] Sakamoto M, Oka K, Morita R and Murakami N 2013 Stable and flexible ring-shaped optical lattice generation by use of axially-symmetric polarization elements *Opt. Lett.* **38** 3661

[29] Takeda M, Ina H and Kobayashi S 1982 Fourier-transform method of fringe-pattern analysis for computer based topography and interferometry *J. Opt. Soc. Am.* **72** 156

[30] Leach J, Yao E and Padgett M J 2004 Observation of the vortex structure of a non-integer vortex beam *New J. Phys.* **6** 71

[31] Jha A K, Jack B, Yao E, Leach J, Boyd R W, Buller G S, Barnett S M, Franke-Arnold S and Padgett M J 2008 Fourier relationship between the angle and angular momentum of entangled photons *Phys. Rev.* A **78** 043810

[32] Eskicioglu A M and Fisher P S 1995 Image quality measures and their performance *IEEE Trans. Commun.* **43** 2959

[33] Boashash B 2003 *Time-Frequency Signal Analysis and Processing: A Comprehensive Reference* (Oxford: Elsevier)